ICSV19
Vilnius, Lithuania
July 08-12, 2012

THE MODES OF A TETHERED, SPHERICAL BALLOON

Kirsty Kuo, Jim Woodhouse and Hugh Hunt

Faculty of Engineering, University of Cambridge, Trumpington St., Cambridge CB2 1PZ, United Kingdom
e-mail: kan26@cam.ac.uk

Observations of a tethered meteorological balloon show that a strong vibration coupling exists between axial forcing of the tether and ovalling deformations of the balloon. Such coupling may lead to system instabilities and fatigue failure in a tethered-balloon system. This is particularly relevant in the case of a balloon launched from a moving vessel, as is proposed as part of the SPICE geoengineering project. This paper investigates the vibration characteristics of a tethered, spherical balloon using a simple analytical model: a tensioned, spherical membrane attached to a spring. The analytical solution for the natural frequencies and modeshapes of this system is compared to transfer functions obtained by laser vibrometry. These results are then used to determine the most suitable method of modelling the dynamic response of a tethered balloon.

1. Introduction

The SPICE geoengineering project is investigating the technical feasibility of using tethered balloons to pump reflective aerosol particles into the atmosphere. Of particular concern to the engineers working on this project is the dynamic behaviour of the tethered-balloon system when subject to variable wind loadings along its 20km length, and base excitations when launched from a moving vessel. These wind loadings and base excitations may produce waves that travel along the tether, resulting in instabilities and fatigue problems.

Preliminary investigations of a tethered-balloon system, using a 1m-diameter meteorological balloon tethered at 15m, were conducted as part of the SPICE project. During these small-scale tests a strong vibration coupling between the tether and the balloon was observed. Base excitation of the tether at specific frequencies in the axial direction was seen to result in ovalling deformations of the balloon. As no record of these tether-balloon couplings could be found in the literature, this paper aims to investigate this effect further, using simple dynamic models and experimental testing.

Recent papers on the dynamics of high-altitude tethered balloons [1-4] treat the balloon as a rigid body. The spherical or streamlined shape of the balloon affects the lift and drag forces, but the forces from the tether are assumed to result in no balloon deformations. In this paper, the balloon is assumed to have a spherical shape. This is the simplest balloon shape, and is a good approximation to the shape of meteorological balloons and small-scale high-altitude balloons. Streamlined aerostats that exhibit weather-vaning behaviour, and the pumpkin-shaped envelopes that are designed to reduce hoop stresses in large high-altitude balloons are considered beyond the scope of this paper. The tether is assumed to be subject only to those forces exerted by the balloon or the base excitation; no effects due to wind are considered.

Analogous studies of the vibration modes of thin-walled spherical shells include those with application to inflatable cushions [5]; pneumatic tires [6]; eyeballs [7]; heart ventricles [8], soap bubbles [9-10]; and basketballs [11]. These studies use a combination of one or more of analytical techniques, finite element analysis and experimental measurement to determine modeshapes and natural frequencies. The approach used in this paper is to model the spherical balloon using the analytical solution for a spherical shell, attached to the balloon neck that is modelled as a spring in axial vibration. The calculated natural frequencies and modeshapes are then compared to those observed during experimental testing, and conclusions regarding the suitability of this model are made.

2. Experiment

The aim of the experimental part of this work was to obtain the frequency response function (FRF) of a spherical balloon at the base of the balloon, near the point at which a tether could be attached. A large, spherical, helium-filled novelty balloon was used as the test piece, and the driving-point response was obtained using a impact hammer and a laser vibrometer. The balloon is made of rubber latex, and has a design diameter of 1m, though was only partially inflated for ease of handling. The laser vibrometer is a Polytec OFV302 single-point vibrometer, connected through a Polytec OFV 3001 vibrometer controller. The velocity range is 1000mm/s/V and the velocity filter is set at 2.4kHz. The impact hammer is a miniature instrumented impact hammer, model PCB 086E80.

The experimental parameters are given in Table 1, and a photograph of the experimental setup is shown in Fig. 1. Using the balloon skin mass and the balloon dimensions, the density of the balloon ρ was calculated to be 530kgm^{-3}. The stiffness of the balloon neck was determined to be 49N/m by placing small weights on the balloon and measuring the static deflection. The pressure in the balloon was measured using a U-tube manometer.

The balloon was restrained by a clamp on the neck of the balloon, below the tie-off point. The impact hammer was used to deliver an impulse to the base of the balloon, near the neck, and the laser beam was aimed at a piece of reflective tape positioned as close as possible to the impact point. The data from the impact hammer and the laser vibrometer were logged and analysed using customised Matlab program. A total of 50 hammer impacts were used to calculate an averaged velocity FRF, which is shown together with the associated coherence in Fig. 2. The first eight major peaks of this FRF occur at 0.63Hz, 6.8Hz, 55.1Hz, 79.8Hz, 105Hz, 131Hz, 157Hz, and 185Hz, and the modal ratios for these peaks are given in Table 2. A series of smaller peaks lie at 10.4Hz, 14.3Hz, 24.6Hz and 36.3Hz. The coherence lies between 0.9 and 1.0 at each of the peak frequencies up to 300Hz, hence the resonant behaviour of the balloon in this range is due to the hammer impact.

Table 1. Experimental parameters.

Parameter	Symbol	Value
Uninflated balloon radius	a_0	0.101m
Inflated balloon radius	a	0.32m
Uninflated balloon thickness	h_0	5x10^{-4}m
Inflated balloon thickness	h	5x10^{-5}m
Neck stiffness	k	49Nm^{-1}
Balloon skin mass	m	3.5x10^{-2}kg
Internal pressure (gauge)	$p - p_0$	1.27 x10^{3}Pa
Atmospheric pressure	p_0	1.03x10^{5}Pa
Atmospheric temperature		291K

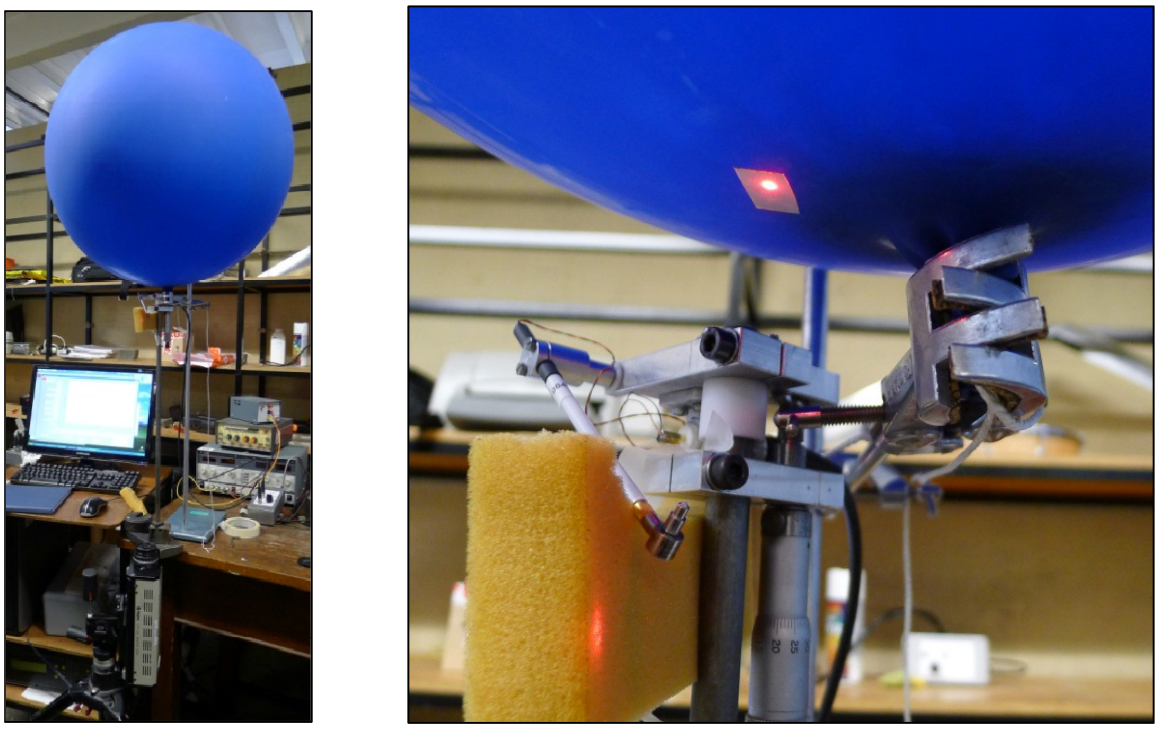

(a) (b)

Figure 1. (a) Experimental setup used to determine balloon frequency response function; (b) Close-up of the impact hammer and measurement points.

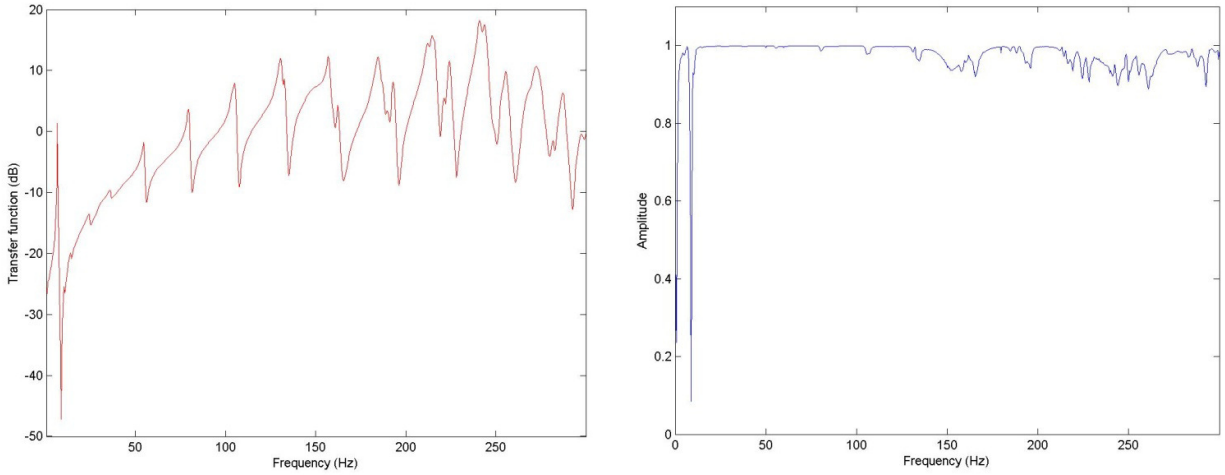

(a) (b)

Figure 2. (a) The driving-point FRF; and (b) the corresponding coherence.

Table 2. The measured modal ratios for the balloon .

Frequency Ratio	$\frac{\omega_2}{\omega_1}$	$\frac{\omega_3}{\omega_2}$	$\frac{\omega_4}{\omega_3}$	$\frac{\omega_5}{\omega_4}$	$\frac{\omega_6}{\omega_5}$	$\frac{\omega_7}{\omega_6}$
Model	8.1	1.44	1.32	1.25	1.20	1.18

3. Modelling

In this section, a mathematical model for the dynamic behaviour of the balloon is described, and the theoretical driving-point velocity FRF is calculated for comparison with the experimental results.

The balloon is best characterised as a thin-walled spherical membrane, subject to a uniform internal pressure that results in tensile stresses within the spherical wall. For a thin-walled sphere of radius a and thickness h, a first approximation to σ, the surface tension in the balloon skin, can be obtained using the Young-Laplace formula for soap bubbles:

$$p - p_0 = \frac{4\sigma}{a} \tag{1}$$

where $p - p_0$ is the pressure difference across the membrane.

A more accurate representation of the surface tension in a balloon is obtained by considering the characteristics of the constituent material. For a rubber or latex balloon, the membrane material is incompressible and has a stress-stretch relationship that is characteristic of a Mooney-Rivlin material. This results in the equation [12]

$$\sigma = \frac{1}{2} s_+ h_0 \left(1 - \left(\frac{a_0}{a}\right)^6\right)\left(1 - \frac{s_-}{s_+}\left(\frac{a}{a_0}\right)^2\right), \tag{2}$$

where material coefficients $s_+ = 300\text{kPa}$ and $s_- = -30\text{kPa}$, and h_0 and a_0 are the thickness and radius of the uninflated balloon, respectively.

Using the experimental parameters given in Table 1, the surface tension is calculated as 103Nm^{-1} using Eq. 1, and 152Nm^{-1} using Eq. 2. There is a significant difference between these two results, hence it is recommended that the latter equation is used when modelling balloon vibrations.

3.1 Vibration of balloon skin

As the balloon skin is thin and taut, it is expected that it will exhibit vibration behaviour that is primarily governed by the surface tension in the membrane. The bending stiffness and material damping of the membrane is assumed to be negligible, and it is assumed that there is no variation in the thickness of the balloon skin. The surrounding air is assumed to be inviscid and incompressible.

An analytical solution for such a system is found in the literature, in the area of small oscillations of soap bubbles. The model used in this paper is based on the solution proposed by Grinfeld [10], which differs from Lamb's well-known solution [13] in that it includes the inertia of the bubble film, and oscillations in the thickness of the film. Grinfeld begins with the linearised form of Euler's equations governing inviscid flow

$$\frac{\partial v^i}{\partial t} = -\frac{1}{\rho}\nabla^i p \tag{3a}$$

$$\nabla_i v^i = 0, \tag{3b}$$

where v^i is the covariant component of the velocity fields, ρ is the surrounding fluid density and p is the pressure. The momentum and velocity components in each of the three spherical coordinate directions are derived, and the condition that the ambient velocity field in the radial direction must be equal on either side of the bubble film is applied. The bubble film is incorporated using a Laplace capillarity model and specially derived linearised equations for the dynamics of the film, resulting in a dispersion relationship. Neglecting oscillations in the thickness of the film, the solution to the dispersion equations gives the natural frequencies ω_j of the soap bubble as

$${\omega_j}^2 = \frac{\sigma}{a^3}\frac{(j-1)j(j+1)(j+2)}{j(j+1)\tau_0 a^{-1} + (j+1)\rho^+ + j\rho^-}. \tag{4}$$

τ_0 is the uniform equilibrium two-dimensional mass density of the film, ρ^+ is the fluid density inside the bubble, and ρ^- is the fluid density outside the bubble. As the mass density of the film approaches zero, this equation is shown to reduce to the Lamb solution for small oscillations of a liquid droplet [13].

The corresponding modeshapes are proportional to the surface spherical harmonics, $Y_{jn}(\theta,\varphi)$. In orthonormal form, the surface spherical harmonics are made up of two expressions:

$$\sqrt{\frac{2j+1}{2\pi}\frac{(j-n)!}{(j+n)!}}P_j{}^n(\cos\varphi)\cos n\theta, \text{ and } \sqrt{\frac{2j+1}{2\pi}\frac{(j-n)!}{(j+n)!}}P_j{}^n(\cos\varphi)\sin n\theta \tag{5}$$

where $P_j{}^n(\cos\varphi)$ are associated Legendre functions of the first kind of degree j and order n.

3.2 Calculating the frequency response function

Having obtained the natural frequencies and mode shapes of the tensioned sphere, it is now necessary to determine the driving-point velocity FRF. The transfer function $H(\boldsymbol{z}_r,\boldsymbol{z}_s,\omega)$ of an undamped system at $\boldsymbol{z}_r$ subjected to a unit harmonic input force at $\boldsymbol{z}_s$ is given in Newland [14] as

$$H(\boldsymbol{z}_r,\boldsymbol{z}_s,i\omega)=\sum_{j=0}^{\infty}\frac{U_j(\boldsymbol{z}_r)U_j(\boldsymbol{z}_s)}{{\omega_j}^2-\omega^2} \tag{6}$$

where $U_j(\boldsymbol{z}_r)$ is the mass-normalised mode function of mode j. For the case of the vibrating bubble or balloon skin, the normalised mode function is represented solely by the contribution of the membrane displacement in the radial direction. The mass-normalisation condition is

$$\lambda^2\int_0^{2\pi}\int_0^{\pi}Y_{jn}(\theta,\varphi)\,\rho t a^2 d\varphi d\theta=1, \tag{7}$$

and is evaluated numerically in the modelling program. The driving point velocity transfer function of the balloon at $\boldsymbol{z}_r=\boldsymbol{z}_s=(a,0,0)$ is

$$H_{ball}(\boldsymbol{z}_r,\boldsymbol{z}_s,i\omega)=\sum_{j=0}^{\infty}\frac{i\omega\lambda^2 Y_{jn}(0,0)Y_{jn}(0,0)}{{\omega_j}^2-\omega^2} \tag{8}$$

3.3 The balloon neck

The experimental setup described in Section 2 differs from the free vibration of a tensioned sphere by way of the balloon neck, which can be described as a connection between the balloon and the rigid clamp. The balloon neck is modelled as a linear spring in axial excitation, with a driving-point transfer function H_{neck} of

$$H_{neck}(i\omega)=\frac{1}{k}, \tag{9}$$

where k is the extensional stiffness of the neck. The spring representing the neck is attached to the model of the balloon using the method of joining subsystems, detailed in Newland [14]. The resulting transfer function for the coupled system, H_{coup}, calculated at the point where the sphere attaches to the spring, is

$$H_{coup}=\frac{H_{ball}H_{neck}}{H_{ball}+H_{neck}}. \tag{10}$$

3.4 Results

The experimental parameters given in Table 1 were used to obtain the driving-point velocity transfer function of a tensioned spherical membrane, as expressed in Eq. 8. The results are shown in Fig. 3a. Peaks in the transfer function occur at 0Hz, 0Hz, 27.9Hz, 50.2Hz, 73.9Hz, 99.1Hz, 125Hz, 153Hz and 181Hz. Each of the peaks in this figure represents a cluster of $2j+1$ modes: $j+1$ of these are $\cos n\theta$ modes, and j of these are $\sin n\theta$ modes, as given in Eq. 5. The modeshapes of the peak at 27.9Hz are illustrated in Fig. 4, and it can be seen that the first four modeshapes (a-d) have four longitudinal modal lines, whereas the final modeshape (e) has two latitudinal modal lines.

The effect of incorporating the stiffness of the balloon neck using Eq. 19 is shown in Fig. 3b: the natural frequencies have been shifted slightly to the right. The modal ratios for these first eight modes are given in Table 3. Referring to Eq. 4, these modal ratios are seen to be independent of surface tension, and dependent on balloon radius, material density, and internal & external fluid densities.

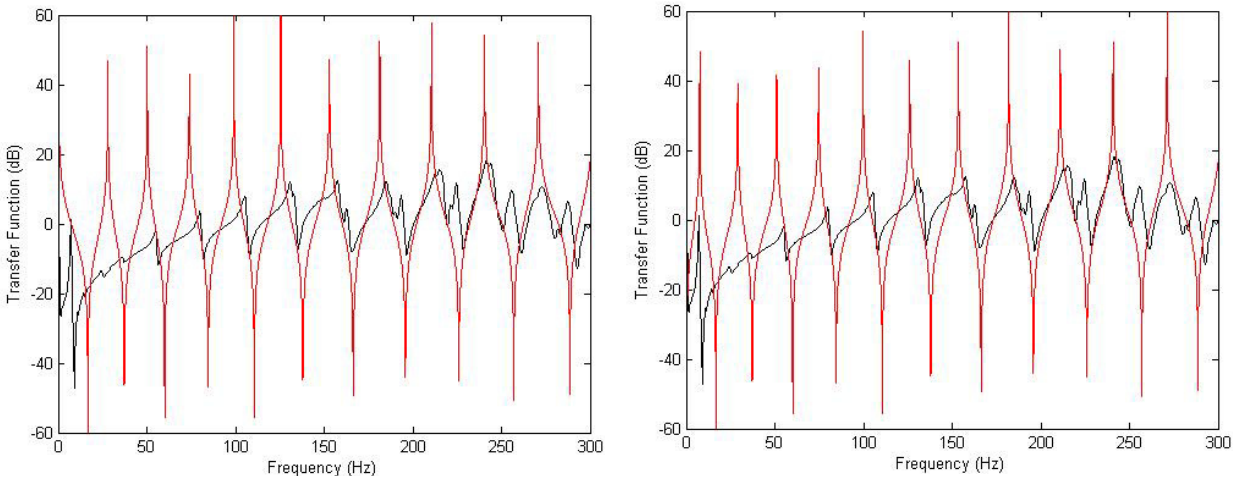

(a) (b)

Figure 3. The driving-point transfer function (in red) predicted by the model for (a) the balloon; and (b) the balloon with incorporated neck stiffness. The black line shows the experimental results from Section 2.

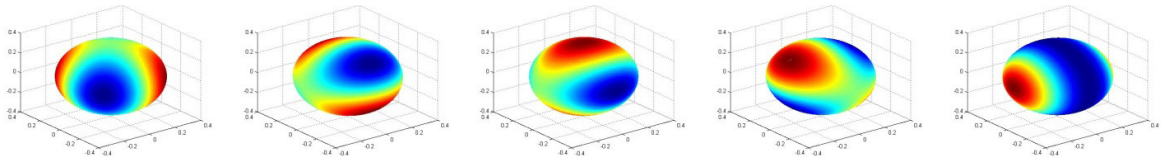

(a) (b) (c) (d) (e)

Figure 4. The five modeshapes found in the modal cluster at 27.9Hz ($\boldsymbol{j = 2}$).

Table 3. The predicted modal ratios for a balloon with incorporated neck stiffness .

Frequency Ratio	$\frac{\omega_2}{\omega_1}$	$\frac{\omega_3}{\omega_2}$	$\frac{\omega_4}{\omega_3}$	$\frac{\omega_5}{\omega_4}$	$\frac{\omega_6}{\omega_5}$	$\frac{\omega_7}{\omega_6}$	$\frac{\omega_8}{\omega_7}$
Model	3.82	1.76	1.46	1.34	1.26	1.22	1.18

4. Discussion

For the particular case of the latex balloon clamped at the base, the breathing mode at $j = 0$ is not expected to be seen, as it is assumed that the gas inside the balloon is incompressible and hence the volume of the balloon is constant. This is consistent with the experimental observations.

The first peak in the experimental results occurs at 0.63Hz, and visual observation of the balloon indicates that this peak corresponds to a low-frequency, lightly damped, rigid-body rocking motion of the balloon about the clamp. The balloon was highly sensitive to air-flow disturbances caused by nearby movements, making it particularly difficult to avoid excitation of this mode. Circle fitting of the experimental results gave a Q-factor of 28.9 for this mode, which corresponds to a damping ratio of 0.017.

The second peak in the experimental results occurs at 6.8Hz, and visual observation of the balloon indicates that this peak corresponds to the theoretical $j = 1$ mode: vertical rigid-body translation of the balloon's centre of mass. Although spherical shell theory predicts that this mode will occur at 0Hz, the natural frequency has been shifted slightly. This is because the balloon's neck and the low-tension material at the base of the balloon are acting together as a 'spring', separating the

balloon from the clamp. As a first estimate, this mode can be considered to represent a one-degree-of-freedom mass-on-a-spring system. The mass of the balloon is taken as the sum of the mass of the balloon skin (0.035kg), the mass of helium (0.023kg) and the added mass of half the displaced air (0.085kg). The stiffness of the balloon neck was determined to be 49N/m, which gives an estimated natural frequency of 3Hz. A better prediction of this natural frequency is obtained by incorporating the stiffness of the balloon neck into the balloon model using Eq. 19. This results in a predicted natural frequency of 7.6Hz, which is within 11% of the measured value.

Initial examination of Fig. 3(b) and comparison of the mode spacings in Table 2 and Table 3 indicate that the natural frequencies at $j \geq 3$ align very well with the experimental results, suggesting that the $j = 2$ mode has not been excited by this experimental setup. To investigate this further, the balloon was excited using an amplifier and speaker system at a pure tone that matched each of the natural frequencies. Visual and tactile observation of the balloon's vibrations indicated that the 55.1Hz mode has two latitudinal modal lines, arranged identically to the $j = 2$ modeshape shown in Figure 4(e). This suggests that the natural frequency at 55.1Hz is due to the $j = 2$ modeshape. The number of latitudinal modal lines increased linearly as the pure tone was matched to the higher natural frequencies: three modal lines at 79.8Hz ($j = 3$), four at 105Hz ($j = 4$), and five at 131Hz ($j = 5$). The reason for the discrepancy between the modelling predictions and the experimental results is currently under further investigation; an early hypothesis is that this may be caused by the high degree of inhomogeneity in the balloon skin.

It can be seen in Fig. 2(a) that as the frequency increases, the major peaks begin to separate into clusters of closely-spaced peaks. This separation is due to the inhomogeneity of the balloon, which has a more pronounced effect on higher frequencies as the modal displacement variation occurs over shorter distances. Inhomogeneity exists in the shape of the balloon (as seen in Fig. 1(a)), the thickness of the balloon skin (seen in Fig. 1(b)), and the surface tension in the balloon skin.

Although the mathematical model used in this paper has not been effective in accurately predicting the higher-order natural frequencies of the balloon, a reasonable estimate of the 'bounce' mode has been obtained. By using appropriate scaling of the balloon and fluid parameters, this same model can be applied to larger scale balloons to obtain a first estimate of this natural frequency.

5. Conclusion

This paper has explored the vibration behaviour of a spherical latex balloon using both mathematical modelling and experimental testing. Impact-hammer testing and laser vibrometry identified the primary modes of vibration: two rigid-body modes, and a series of higher-order modes with latitudinal modal lines. An analytical model for soap bubbles was used as the basis for the balloon model, with the inclusion of a stiffness element to represent the balloon neck. This model gave a reasonable prediction of the rigid-body 'bounce' mode, but under-predicted the natural frequencies of the higher-order modes. It is proposed that inhomogeneities dominate the vibration response of the balloon, and further work exploring this area is being undertaken.

Acknowledgements

The authors would like to thank Professor C.R. Calladine FRS of the University of Cambridge Department of Engineering and Professor J.R. Lister of the University of Cambridge Department of Applied Mathematics and Theoretical Physics who provided valuable comments on this research. This work has been funded by the Engineering and Physical Sciences Research Council UK, reference EP/IO1473X/1.

REFERENCES

1. G.S. Aglietti, "Dynamic response of a high-altitude tethered balloon system", *Journal of Aircraft,* **46**(6), 2032-2040 (2009).
2. K.A. Stanney and C.D. Rahn, "Response of a tethered aerostat to simulated turbulence", *Communications in Nonlinear Science and Numerical Simulation*, **11**, 759-776 (2006).
3. C. Lambert and M. Nahon, "Stability analysis of a tethered aerostat", *Journal of Aircraft*, **40**(4), 705-715 (2003).
4. P. Coulombe-Pontbriand and M. Nahon, "Experimental testing and modelling of a tethered spherical aerostat in an outdoor environment", *Journal of Wind Engineering and Industrial Aerodynamics*, **97**, 208-218 (2009).
5. L.E. Penzes and H. Kraus, "Free vibration of an inflated oblate spheroidal shell", *Journal of Sound and Vibration*, **27**(4), 559-572 (1973).
6. L.E. Kung, W. Soedel and T.Y. Yang, "Free vibration of a pneumatic tire-wheel unit using a ring on an elastic foundation and a finite element model", Journal of Sound and Vibration, **107**(2), 181-194 (1986).
7. L. Coquart, C. Depeursinge, A. Curnier and R. Ohayon, "A fluid-structure interaction problem in biomechanics: prestressed vibrations of the eye by the finite element method", *Journal of Biomechanics*, **25**(10), 1105-1118 (1992).
8. A. Singer, "Computed ventricular acoustic frequency", *Bulletin of Mathematical Biophysics*, **29**, 465-471 (1967).
9. G. Rämme, "Modelling the atom by rotating and vibrating soap bubbles", *Physics Education*, **29**, 313-318 (1994).
10. P. Grinfeld, "Small oscillations of a soap bubble", *Studies in Applied Mathematics*, **128**(1), 30-39 (2012).
11. D. Russell, "Basketballs as spherical acoustic cavities", *American Journal of Physics*, **78**(6), 549-554 (2010).
12. I. Müller and P. Strehlow, *Rubber and Rubber Ballooons: Paradigms of Thermodynamics*, Lect. Notes Phys. **637**, Springer-Verlag Berlin Heidelberg, 2004.
13. H. Lamb, *Hydrodynamics*, Dover Publications, New York, 1993.
14. D.E. Newland, *Mechanical Vibration Analysis and Computation*, Dover Publications, Inc. Mineola, 1989.